



Computing overall elastic constants of polydisperse particulate composites from microtomographic data

Hyunsun Lee^{b,1}, Andrew S. Gillman^a, Karel Matouš^{a,*}

^a Department of Aerospace and Mechanical Engineering, University of Notre Dame, Notre Dame, IN 46556, USA

^b Department of Mathematics, Florida State University, Tallahassee, FL 32306, USA

ARTICLE INFO

Article history:

Received 7 October 2010

Received in revised form

17 May 2011

Accepted 19 May 2011

Available online 26 May 2011

Keywords:

Hashin–Shtrikman–Willis variational principle

Anisotropic material response

Polydisperse particulate composites

Adaptive sparse Smolyak quadrature

Microtomography

ABSTRACT

In this paper, we use the well-known Hashin–Shtrikman–Willis variational principle to obtain the overall mechanical properties of heterogeneous polydisperse particulate composites. The emphasis is placed on the efficient numerical integration of complex three-dimensional integrals and on aspects of the anisotropic material response of real tomographically characterized packs. For this purpose, we numerically calculate the complete statistics of real packs, which are numerically or tomographically generated. We use the parallel adaptive sparse Smolyak integration method with hierarchical basis to integrate complex singular integrals containing the product of probability functions and the second derivative of Green's function. Selected examples illustrate both the numerical and physical facets of our work. First, we show the reduction of integral points for integration in spherical coordinates. Then, we comment on the parallel scalability of our method and on the numerical accuracy associated with the integration of a singular function. Next, we validate the solver against the experimental data and verify the results by comparing it to a closed-form expression. To investigate the ability of our scheme to capture the anisotropic nature of packs, we study a lattice type system. Finally, we report on the elastic constants computed for the modeled anisotropic particulate system that is tomographically characterized.

© 2011 Elsevier Ltd. All rights reserved.

1. Introduction

How to compute the effective properties of heterogeneous materials has been a long standing quest, and many multiscale techniques that can link physical phenomena across various scales have been proposed over past several decades to fulfill it. Among those, the seminal work of Hashin and Shtrikman (1962), Willis (1977), Bensoussan et al. (1978), Hill (1985), Torquato (1997) and Arns et al. (2003) deserve attention, but many others contributed to this effort also (Castaneda, 1998; Christensen and Lo, 1979; Dvorak and Srinivas, 1999; Fullwood et al., 2008; Ranganathan and Ostoja-Starzewski, 2008; Šejnoha and Zeman, 2002; Walpole, 1969).

Recently, imaging techniques that are common in medical practice have become very popular in materials science as well. Three-dimensional microtomography (micro-CT) has especially led to vast expansion of statistical modeling techniques that investigate the morphology of widely used material systems and its impact on the overall mechanical

* Corresponding author. Tel.: +1 574 631 1376; fax: +1 574 631 8341.

E-mail address: kmatous@nd.edu (K. Matouš).

¹ The initial work was performed when H. Lee was a postdoctoral scholar in K. Matouš' research group at the University of Illinois at Urbana-Champaign.

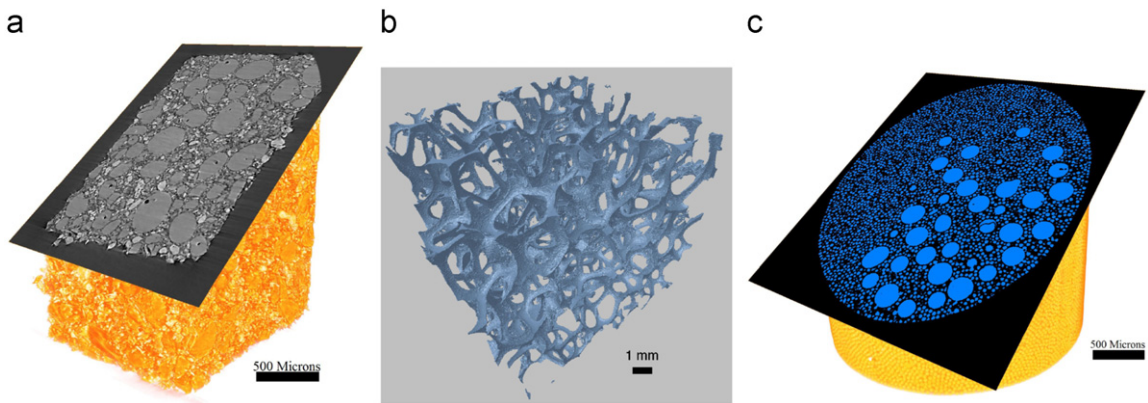


Fig. 1. Typical members of the micro-CT based ensemble. (a) Heterogeneous propellant. (b) Synthetic foam. (c) Glass beads.

and transport properties. We aim to work on solid propellants (Gallier and Hiernard, 2008), glass beads (Lee et al., 2009), paper (Rolland du Roscoat et al., 2007), Fontainebleau sandstone (Arns et al., 2002) and engineered cementitious composites (Bouvard et al., 2007), just to name a few. An example of the complicated microstructures obtained from micro-CT can be seen in Fig. 1.

The importance of the higher-order statistics and their influence on the overall material behavior start with early work of Bernal (1959) who investigated the geometrical structure of liquids using the radial distribution function. In condensed matter physics, the work of Willis (1977) is especially important since it provides a direct link between statistics and mechanical properties (Hashin–Shtrikman–Willis variational principle). Third-order models of nonlinear composites have also been proposed (Castaneda, 1998; Talbot and Willis, 1985; Willis, 1986). The assessment of mechanical and transport properties by the Hashin–Shtrikman–Willis approach relies on the computation of certain mechanical concentration tensors, which are functions of material morphology and depend on the information transfer through it. We now note that the integration of the mechanical concentration tensors, which are the basic building blocks of this technique, is strenuous. Moreover, obtaining detailed statistical information in three-dimensions of real polydisperse systems is laborious.

For the third-order model, the mechanical tensors are computed through double three-dimensional integration of complex integrands, which are products of the second derivative of Green's function, Γ , and the third-order probability functions $S_{rsq}(\mathbf{x}, \mathbf{x}', \mathbf{x}'')$. For the second-order model, complexity still remains as Γ interacts with the second-order probability functions $S_{rs}(\mathbf{x}, \mathbf{x}')$ in three-dimensions. Therefore, in many previous works, specific assumptions about the shape and the orientation of inclusions have been considered (Willis, 1977), and most of the work has been done in two-dimensions (Šejnoha and Zeman, 2002) using artificial or statistically isotropic probability functions (Castaneda, 1998; Drugan, 2003; Torquato, 1987). Some nonlocal Hashin–Shtrikman–Willis models are limited to only two-phase composites (Drugan, 2003). The attempt has been also made to integrate in the Fourier domain (Drugan, 2003; Drugan and Willis, 1996) and to assess the probability functions on a pixel/voxel basis (Fullwood et al., 2008; Šejnoha and Zeman, 2002). Unfortunately, voxel-based representation from micro-CT data requires very large data sets, our data consist of ~ 66 million voxels, as has been pointed out in our previous work (Lee et al., 2009). Moreover, the discrete fast Fourier transform is not easily parallelizable (Matteo and Johnson, 2005). Many of these issues, especially related to difficulties in obtaining real probability functions and linking them with statistical micromechanics approaches, are discussed in the work of Willis (1986) and Torquato (1987).

Therefore, one would like to have the ability to compute properties of polydisperse composites directly without limits on the complexity of the probability spectrum and multidimensionality, and with statistics that are directly and accurately computed from micro-CT scans. This is a focus of this paper. In this work, we consider systems with inclusions of arbitrary size and orientation and focus on efficient numerical integration with realistic statistics, which allows us to accurately capture the underlying three-dimensional anisotropic nature of particulate polydisperse systems. We employ an adaptive sparse Smolyak integration scheme with hierarchical basis and exploit the geometrical characteristics of our integrand, i.e., we use spherical coordinates to define the basis functions and the integration. The integration scheme is further parallelized. We resolve the probability spectrum accurately without assumptions on its structure and with very small errors as has been shown in Lee et al. (2009). The combination of these advances allows us to compute the mechanical properties with higher fidelity directly from micro-CT data. Material anisotropy due to the microstructure of a composite is accurately captured. Several examples are selected to demonstrate both the computational and physical facets of our work. First, we summarize well-established concepts of statistical descriptors and introduce, for the clarity of presentation, the Hashin–Shtrikman–Willis variational principle (Section 2). Next, we introduce a sparse Smolyak integration scheme to evaluate complex mechanical concentration tensors (Section 3). Finally, we verify and validate our solver and demonstrate its capability to assess mechanical properties of systems that are characterized by micro-CT (Section 4). The conclusions are drawn in Section 5.

2. Theoretical model

We use the well-known Hashin–Shtrikman variational principle (Hashin and Shtrikman, 1962) in the modified form presented by Willis (1977) to compute the overall elastic constants of a heterogeneous composite. This variational principle was later extended by Šejnoha and Zeman (2002), and Prochazka and Šejnoha (2004) by introducing eigenstrains (stress free strains). It is known that the effective properties of a heterogeneous material do not depend only on the properties of each phase, but also on the interactions between the material phases. In a statistical sense, both the volume fraction of each phase and various correlation functions between the phases are fundamental in determining the material properties (Talbot and Willis, 1985; Torquato, 2002). In this section, we introduce the probability functions and governing equations for completeness of the presentation.

2.1. Review of basic statistical descriptors

To describe the probability functions, we consider a phase indicator function at a position \mathbf{x} in a sample α of an ensemble space \mathcal{E} :

$$\chi_r(\mathbf{x}; \alpha) = \begin{cases} 1 & \text{if } \mathbf{x} \text{ in phase } r, \\ 0 & \text{otherwise.} \end{cases} \quad (1)$$

The ensemble average is given by

$$\overline{\chi_r(\mathbf{x})} = \int_{\mathcal{E}} \chi_r(\mathbf{x}; \alpha) p(\alpha) d\alpha, \quad (2)$$

where $p(\alpha)$ is a probability density function of α in \mathcal{E} . The n -point probability function, $S_{r_1 r_2 \dots r_n}(\mathbf{x}_1, \mathbf{x}_2, \dots, \mathbf{x}_n)$, is defined as

$$S_{rs\dots q}(\mathbf{x}_1, \mathbf{x}_2, \dots, \mathbf{x}_n) = \overline{\chi_r(\mathbf{x}_1) \chi_s(\mathbf{x}_2) \cdots \chi_q(\mathbf{x}_n)}, \quad (3)$$

and it represents the probability of finding phases r, s, \dots, q at points $\mathbf{x}_1, \mathbf{x}_2, \dots, \mathbf{x}_n$, simultaneously. In our work, we use the second-order model that includes one- and two-point probability functions.

In general, the probability functions for a heterogeneous material are spatially complex. A common assumption is that of statistical homogeneity, where the probability functions are translationally invariant. For statistical homogeneous materials, the one-point probability function is a constant value, $S_r(\mathbf{x}) = c$, and the two-point function simplifies to $S_{rs}(\mathbf{x}, \mathbf{x}') = S_{rs}(\mathbf{x} - \mathbf{x}')$. When considering statistically homogeneous systems, it is meaningful to define volume averages. Under the ergodic assumption for homogeneous systems, ensemble averaging is equivalent to volume averaging in the infinite volume limit as described by the following equation

$$S_{rs\dots q}(\mathbf{x}_1, \mathbf{x}_2, \dots, \mathbf{x}_n) = \lim_{V \rightarrow \infty} \left(\frac{1}{V} \int_V \chi_r(\mathbf{x}_1 - \mathbf{d}) \chi_s(\mathbf{x}_2 - \mathbf{d}) \cdots \chi_q(\mathbf{x}_n - \mathbf{d}) dV \right), \quad (4)$$

where \mathbf{d} is the translation vector. With these simplifications, the one-point probability function is reduced to the volume fraction $S_r(\mathbf{x}) = c_r$ of phase r . An additional simplification is that of statistical isotropy, where the probability functions are rotationally invariant. The two-point probability functions of a statistically homogeneous and isotropic system are defined as $S_{rs}(\mathbf{x}, \mathbf{x}') = S_{rs}(|\mathbf{x} - \mathbf{x}'|)$, where the function only depends on the distance between two points. In addition, we observe the limit cases in the pointwise sense of the two-point isotropic probability functions which can be expressed as

$$S_{rs}(|\mathbf{x} - \mathbf{x}'|) \rightarrow \begin{cases} c_r \delta_{rs} & \text{if } |\mathbf{x} - \mathbf{x}'| \rightarrow 0, \\ c_r c_s & \text{if } |\mathbf{x} - \mathbf{x}'| \rightarrow \infty, \end{cases} \quad (5)$$

where δ_{rs} is the Kronecker delta. More information on statistical descriptors can be found in books by Torquato (2002) and Beran (1968). In this work, we use both complete, $S_{rs}(\mathbf{x} - \mathbf{x}')$, and isotropic, $S_{rs}(|\mathbf{x} - \mathbf{x}'|)$, probability functions to address the issues of the material anisotropy. Details on how we compute the n -point probability functions from micro-CT data are given in Lee et al. (2009).

2.2. Governing equations

Let \mathbf{u} , $\boldsymbol{\sigma}$, $\boldsymbol{\varepsilon}$ and \mathbf{L} be the displacement vector, the second-order stress tensor, the second-order strain tensor, and the fourth-order elasticity tensor, respectively. We start with the local constitutive law of a given constituent at point \mathbf{x} in a representative volume element (RVE) that reads

$$\boldsymbol{\sigma} = \mathbf{L}(\boldsymbol{\varepsilon} - \boldsymbol{\mu}), \quad \boldsymbol{\sigma} = \mathbf{L}\boldsymbol{\varepsilon} + \boldsymbol{\lambda}, \quad (6)$$

where $\boldsymbol{\mu} = -\mathbf{L}^{-1}\boldsymbol{\lambda}$ and $\boldsymbol{\lambda}$ denote eigenstrain and eigenstress, respectively. The eigenstrain field introduced here represents the stress free strain induced in the system by thermal and/or inelastic effects (e.g., plasticity, decohesion (Matouš, 2003)).

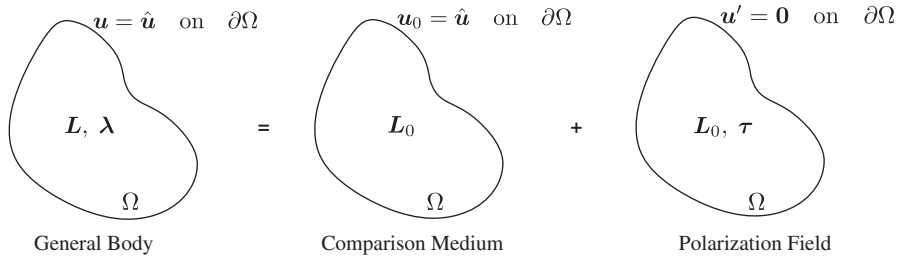


Fig. 2. Body decomposition with prescribed boundary conditions. Note that $\hat{\mathbf{u}} = \boldsymbol{\varepsilon}_0 \cdot \mathbf{x}$.

Hashin and Shtrikman (1962), in their seminal work proposed the body decomposition, as shown in Fig. 2, with the displacement and strain fields split as follows:

$$\begin{aligned} \mathbf{u}' &= \mathbf{u} - \mathbf{u}_0 \quad \text{in } \Omega, \\ \boldsymbol{\varepsilon}' &= \boldsymbol{\varepsilon} - \boldsymbol{\varepsilon}_0 \quad \text{in } \Omega, \\ \mathbf{u}' &= \mathbf{0} \quad \text{on } \partial\Omega, \end{aligned} \tag{7}$$

and introduced the symmetric stress polarization tensor, $\boldsymbol{\tau}$, such that

$$\boldsymbol{\sigma} = \mathbf{L}_0 \boldsymbol{\varepsilon} + \boldsymbol{\tau}, \tag{8}$$

where \mathbf{L}_0 is the stiffness tensor of a homogeneous comparison medium, $\boldsymbol{\varepsilon}_0$ denotes the strain tensor in a homogeneous comparison medium, and \mathbf{u}_0 and \mathbf{u}' represent the homogeneous and fluctuation displacement fields, respectively. The polarization field captures the heterogeneous and sometimes anisotropic nature of the material.

The objective is to formulate a variational principle describing the behavior of the inhomogeneous and anisotropic material subjected to known eigenstresses and prescribed boundary displacements (Prochazka and Šejnoha, 2004; Šejnoha and Zeman, 2002; Willis, 1977). The governing equations of the elliptic boundary value problem are given by

$$\begin{aligned} \nabla \cdot [\mathbf{L}_0 \boldsymbol{\varepsilon} + \boldsymbol{\tau}] &= \mathbf{0} \quad \text{in } \Omega, \\ \boldsymbol{\tau} - [\mathbf{L} - \mathbf{L}_0] \boldsymbol{\varepsilon} - \boldsymbol{\lambda} &= \mathbf{0} \quad \text{in } \Omega, \\ \mathbf{u}' &= \mathbf{0} \quad \text{on } \partial\Omega. \end{aligned} \tag{9}$$

A formulation equivalent to one described by the strong form (9) can be obtained by minimizing a certain extended functional (Prochazka and Šejnoha, 2004; Šejnoha and Zeman, 2002)

$$2\mathcal{F}(\boldsymbol{\tau}) = \int_{\Omega} \left[(\boldsymbol{\tau} - \boldsymbol{\lambda}) : [\mathbf{L} - \mathbf{L}_0]^{-1} : (\boldsymbol{\tau} - \boldsymbol{\lambda}) + \boldsymbol{\tau} : \int_{\Omega_{\mathbf{x}'}} \Gamma(\mathbf{x}, \mathbf{x}') : [\boldsymbol{\tau}(\mathbf{x}') - \bar{\boldsymbol{\tau}}] d\Omega_{\mathbf{x}'} - 2\boldsymbol{\tau} : \boldsymbol{\varepsilon}_0 - \boldsymbol{\lambda} : \mathbf{L}^{-1} : \boldsymbol{\lambda} \right] d\Omega, \tag{10}$$

where $\Gamma(\mathbf{x}, \mathbf{x}')$ is the linear operator related to the infinite homogeneous Green's function and $\bar{\boldsymbol{\tau}}$ represents the mean value of $\boldsymbol{\tau}$ (Willis, 1977). The product of the Green's function and the polarization field carries the information about the material morphology (statistics). For ergodic systems (Eq. (4)), the macroscopic (overall) stress and strain tensors are computed by volume averaging

$$\bar{\boldsymbol{\sigma}} = \frac{1}{\Omega} \int_{\Omega} \boldsymbol{\sigma} d\Omega, \quad \bar{\boldsymbol{\varepsilon}} = \frac{1}{\Omega} \int_{\Omega} \boldsymbol{\varepsilon} d\Omega, \tag{11}$$

where

$$\bar{\boldsymbol{\varepsilon}} \equiv \boldsymbol{\varepsilon}_0, \quad \text{since } \int_{\Omega} \boldsymbol{\varepsilon}' d\Omega = \mathbf{0}. \tag{12}$$

Using the formulation highlighted above, the following homogenized macroscopic stress–strain constitutive law can be derived,

$$\begin{aligned} \bar{\boldsymbol{\sigma}} &= \mathbf{L}_0 \bar{\boldsymbol{\varepsilon}} + \bar{\boldsymbol{\tau}}, \\ \bar{\boldsymbol{\sigma}} &= \bar{\mathbf{L}} \bar{\boldsymbol{\varepsilon}} + \bar{\boldsymbol{\lambda}} \equiv \bar{\mathbf{L}} (\bar{\boldsymbol{\varepsilon}} - \bar{\boldsymbol{\mu}}), \end{aligned} \tag{13}$$

where $\bar{\mathbf{L}}$ denotes the macroscopic homogenized secant modulus and $\bar{\boldsymbol{\mu}} = -\bar{\mathbf{L}}^{-1} \bar{\boldsymbol{\lambda}}$ is the macroscopic eigenstrain. The eigenstrains can be used, among other things, to compute the homogenized coefficients of thermal expansion.

2.3. Discrete Hashin–Shtrikman–Willis variational principle

To find a second-order approximation to the stationary point of (10), Willis adopted a piecewise constant trial polarization stress

$$\boldsymbol{\tau}^*(\mathbf{x}) = \boldsymbol{\tau}^*(\mathbf{x}; \alpha) = \sum_{r=1}^n \boldsymbol{\tau}_r \chi_r(\mathbf{x}; \alpha), \tag{14}$$

where $\boldsymbol{\tau}_r$ is constant over the phase r as depicted in Fig. 3, and n represents the number of phases in the composite. In the same manner, the eigenstress field can be expressed as

$$\boldsymbol{\lambda}^*(\mathbf{x}) = \boldsymbol{\lambda}^*(\mathbf{x}; \alpha) = \sum_{r=1}^n \boldsymbol{\lambda}_r \chi_r(\mathbf{x}; \alpha). \tag{15}$$

We use the ergodicity assumption in our work (Eq. (4)), and thus, we perform the volume averages and omit α hereafter.

After introducing discretization of $\boldsymbol{\tau}^*$ and $\boldsymbol{\lambda}^*$ into (10), averaging over the ensemble space \mathcal{E} and using the calculus of variations ($\delta\mathcal{F}$ is the first variation of the functional (10) with respect to $\boldsymbol{\tau}^*$), we obtain the stationary point of the discrete energy principle:

$$\delta\mathcal{F}(\boldsymbol{\tau}^*) = 0, \tag{16}$$

$$c_r(\mathbf{L}_r - \mathbf{L}_0)^{-1} \boldsymbol{\tau}_r + \sum_{s=1}^n \int_{\Omega_{\mathbf{x}'}} \boldsymbol{\Gamma}(\mathbf{x} - \mathbf{x}') (S_{rs}(\mathbf{x} - \mathbf{x}') - c_r c_s) \boldsymbol{\tau}_s \, d\Omega_{\mathbf{x}'} = c_r \bar{\boldsymbol{\epsilon}} + c_r (\mathbf{L}_r - \mathbf{L}_0)^{-1} \boldsymbol{\lambda}_r. \tag{17}$$

The matrix form of the above system for all polarization stresses can be conveniently written as

$$\sum_{s=1}^n \mathcal{A}_{rs} \boldsymbol{\tau}_s = \mathcal{B}_r, \tag{18}$$

where the mechanical concentration tensor \mathcal{A}_{rs} , which does not depend on \mathbf{x}' , states

$$\mathcal{A}_{rs} = \int_{\Omega_{\mathbf{x}'}} \boldsymbol{\Gamma}(\mathbf{x} - \mathbf{x}') (S_{rs}(\mathbf{x} - \mathbf{x}') - c_r c_s) \, d\Omega_{\mathbf{x}'} + c_r (\mathbf{L}_r - \mathbf{L}_0)^{-1} \delta_{rs}, \tag{19}$$

and

$$\mathcal{B}_r = c_r \bar{\boldsymbol{\epsilon}} + c_r (\mathbf{L}_r - \mathbf{L}_0)^{-1} \boldsymbol{\lambda}_r. \tag{20}$$

By solving for $\boldsymbol{\tau}_r$ from (18) and averaging over the phases, we get the overall (mean) polarization stress field as

$$\bar{\boldsymbol{\tau}} = \sum_r c_r \boldsymbol{\tau}_r. \tag{21}$$

Finally, using (13), (19) and (20), we obtain $\bar{\mathbf{L}}$ together with $\bar{\boldsymbol{\lambda}}$.

In his original work, Willis (1977) adopted the assumption of statistical isotropy which simplifies $\int_{\Omega_{\mathbf{x}'}} \boldsymbol{\Gamma}(\mathbf{x} - \mathbf{x}') (S_{rs}(\mathbf{x} - \mathbf{x}') - c_r c_s) \, d\Omega_{\mathbf{x}'}$ to $\mathbf{P}[S_{rs}(\mathbf{0}) - c_r c_s]$, where \mathbf{P} is the polarization tensor originally derived by Eshelby (1957) for isotropic \mathbf{L}_0 . The second form of \mathbf{P} presented in Willis (1977) is for the specific case in which a matrix contains aligned ellipsoids. Both cases assumed no long-range order, where a system is said to possess no long-range order if the events $|\mathbf{x} - \mathbf{x}'| \rightarrow \infty$ for all positions \mathbf{x}

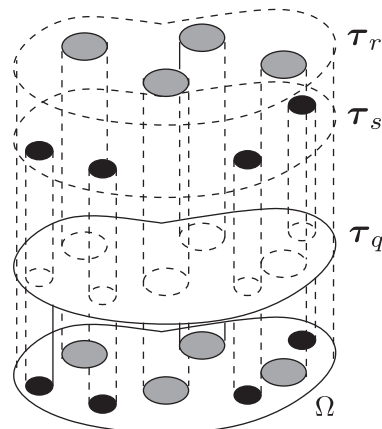


Fig. 3. An example of piecewise constant trial polarization stress field $\boldsymbol{\tau}^*(\mathbf{x})$ for a three-phase composite. The phases r and s are particulate phases and q is the matrix phase. Note that the vertical direction indicates the constant value of polarization stress.

and \mathbf{x}' are statistically independent (Torquato, 2002). It can be shown that a similar result for \mathbf{P} is obtained when one considers only the singular part of the Γ function, such that

$$\Gamma_{kijp}(\mathbf{r}) \simeq \Gamma_{kijp}^s(\mathbf{r}), \tag{22}$$

with

$$\Gamma_{kijp}^s(\mathbf{r}) = \frac{\delta(\mathbf{r})}{3\mu} \left\{ \delta_{kp}\delta_{ij} - \frac{K}{5} (\delta_{kp}\delta_{ij} + \delta_{ki}\delta_{pj} + \delta_{kj}\delta_{pi}) \right\}, \tag{23}$$

where $\mathbf{r} = \mathbf{x} - \mathbf{x}'$, and $\delta(\mathbf{r})$ is the Dirac delta function. Here we use the standard indicial notation, and denote μ the shear modulus and $K = (3\kappa + \mu)/(3\kappa + 4\mu)$, where κ is the bulk modulus, respectively. A suitable choice for the polarization tensor is to use a comparison medium, $\mathbf{P} \equiv \mathbf{P}_0$, where the comparison medium is assumed to be isotropic for this choice of Γ (Eq. (23)).

In the present paper, we also use the piecewise constant trial polarization stress, τ_r . However, instead of the singular approximation, we use the complete form of the Γ function, which accounts for both short and long-range interactions. Furthermore, we numerically evaluate the complex mechanical concentration tensor \mathcal{A}_{rs} using the real, three-dimensional, micro-CT based, first- and second-order statistics. The Γ function, which is related to the second derivative of the Green's function, is defined in our work as

$$\Gamma_{kijp}(\mathbf{r}) = \Gamma_{kijp}^s(\mathbf{r}) + \Gamma_{kijp}^f(\mathbf{r}), \tag{24}$$

where

$$\Gamma_{kijp}^f(\mathbf{r}) = \frac{1}{8\mu\pi} \left\{ \frac{(2-K)\delta_{kp}\delta_{ij} - K(\delta_{pj}\delta_{ki} + \delta_{pi}\delta_{kj})}{|\mathbf{r}|^3} + \frac{(3K-6)r_i r_j \delta_{kp} + 3K(r_p r_j \delta_{ki} + r_k r_j \delta_{pi} + r_p r_k \delta_{ij} + r_i r_p \delta_{kj} + r_i r_k \delta_{pj})}{|\mathbf{r}|^5} - \frac{15K r_i r_j r_k r_p}{|\mathbf{r}|^7} \right\}. \tag{25}$$

In general, the singular part, Γ^s , represents the localized bonds while the formal part, Γ^f , accounts for strain variations within an inclusion from its average value (Fokins and Shermergor, 1969).

We observe that the integration of the mechanical concentration tensor \mathcal{A}_{rs} (Eq. (19)), which is a product of the Gamma function and the second-order probability function, is strenuous especially near the origin due to the singularity of Γ . Although it is difficult to predict the behavior of this integrand, it has some spherical character. This characteristic is used in constructing the numerical integrator. This is described in the following section.

3. Numerical method

To overcome the difficulties with the integration, we use the adaptive sparse-grid Smolyak Integration method with hierarchical basis, which was recently proposed by Ma and Zabarar (2009) for solution of stochastic differential equations. We further extend it to spherical coordinates and parallelize it for our particular problem. The adaptivity of the method reduces the numerical expense that arises due to the complexity of the integrand, and the Smolyak quadrature reduces the complexity present due to the multivariate nature of equations. Integrating using spherical coordinates is natural for our predominantly distance-dependent integrand.

In our work, we follow closely the approach of Ma and Zabarar (2009). For the completeness and clarity of presentation, we describe the fundamentals of an adaptive hierarchical sparse Smolyak method hereafter. A more detailed description can be found in Bungartz and Griebel (2004); Gerstner and Griebel (1998); Smolyak (1963).

3.1. Numerical integration on an adaptive hierarchical sparse grid

Let us consider a smooth function $f : [0, 1]^N \rightarrow \mathbb{R}$. In one-dimension ($N=1$), f can be interpolated as

$$\mathcal{U}^i(f) = \sum_{j=1}^{m_i} f(Y_j^i) a_j^i, \tag{26}$$

where $i \in \mathbb{N}$ (\mathbb{N} —set of all positive integers except zero), $a_j^i \in C([0, 1])$ are the interpolation nodal basis functions, and m_i represents the number of elements of the set X^i of support nodes, Y_j^i :

$$X^i = \{Y_j^i | Y_j^i \in [0, 1] \text{ for } j = 1, 2, \dots, m_i\}. \tag{27}$$

As in Ma and Zabarar (2009), we use hat functions for the basis functions

$$a_1^i = 1, \tag{28}$$

$$a_j^i = \begin{cases} 1 - (m_i - 1)|Y - Y_j^i| & \text{if } |Y - Y_j^i| < 1/(m_i - 1), \\ 0 & \text{otherwise,} \end{cases}$$

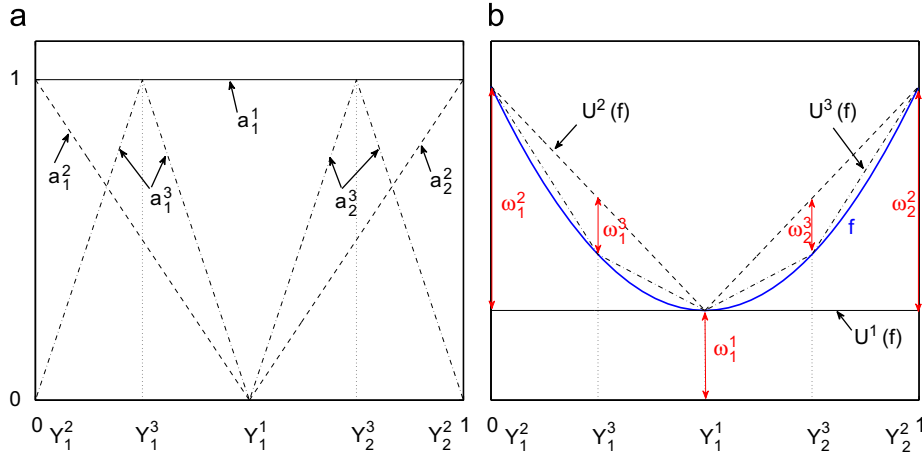


Fig. 4. Hierarchical basis functions in one-dimension and interpolation at level 1,2,3. (a) Basis functions. (b) Interpolation.

for $i > 1$ and $j = 1, \dots, m_i$. The support nodes are defined as

$$m_i = \begin{cases} 1 & \text{if } i = 1, \\ 2^{i-1} + 1 & \text{if } i > 1, \end{cases} \tag{29}$$

$$Y_j^i = \begin{cases} \frac{j-1}{m_i-1} & \text{for } j = 1, \dots, m_i, \text{ if } m_i > 1, \\ 1/2 & \text{for } j = 1, \text{ if } m_i = 1. \end{cases} \tag{30}$$

Fig. 4(a) shows the hierarchical implementation of these nodal basis functions. The building blocks of the Smolyak algorithm for the multivariate case ($N > 1$) are tensor product formulae

$$(\mathcal{U}^{i_1} \otimes \dots \otimes \mathcal{U}^{i_N})(f) = \sum_{j_1=1}^{m_1} \dots \sum_{j_N=1}^{m_N} f(Y_{j_1}^{i_1}, \dots, Y_{j_N}^{i_N})(a_{j_1}^{i_1} \otimes \dots \otimes a_{j_N}^{i_N}). \tag{31}$$

Using those, we can construct the N -dimensional multi-linear basis functions

$$a_j^i(\mathbf{Y}) = a_{j_1}^{i_1} \otimes \dots \otimes a_{j_N}^{i_N} = \prod_{k=1}^N a_{j_k}^{i_k}, \tag{32}$$

where the multi-index $\mathbf{j} = (j_1, \dots, j_N) \in \mathbb{N}^N$, and $j_k, k = 1, \dots, N$ represents the location of a given support node in the k -th dimension from Eq. (30). Here we also denote by \mathbf{i} the multi-index $\mathbf{i} = (i_1, \dots, i_N) \in \mathbb{N}^N$ with $|\mathbf{i}| = i_1 + \dots + i_N$. Note that $i_k, k = 1, \dots, N$ is the level of the interpolation along the k -th direction.

We build the sparse grid interpolation formula by exploiting the incremental structure of the algorithm

$$\begin{aligned} \mathcal{U}^0 &= 0, \\ \Delta^i &= \mathcal{U}^i - \mathcal{U}^{i-1}. \end{aligned} \tag{33}$$

The incremental interpolation formula takes advantage of the nested nature of the grid points, $X^i \subset X^{i+1}$, and leads to formulation of the hierarchical surplus, w_j^i , such that

$$\begin{aligned} \Delta^i(f) &= \sum_{Y_j^i \in X_A^i} a_j^i(f(Y_j^i) - \mathcal{U}^{i-1}(f)(Y_j^i)), \\ &= \sum_{j=1}^{m_A^i} a_j^i \underbrace{(f(Y_j^i) - \mathcal{U}^{i-1}(f)(Y_j^i))}_{w_j^i}, \end{aligned} \tag{34}$$

where $X_A^i = X^i \setminus X^{i-1}$ and $m_A^i = m_i - m_{i-1}$ since $X_{i-1} \subset X_i$. The second equation in (34) is obtained by consecutively numbering the elements in X_A^i and denoting the j -th point of X_A^i as Y_j^i . Fig. 4 shows the hierarchical hat functions and the interpolation in one-dimension including the surplus w_j^i .

For the multivariate case, the sparse interpolant, using the product formula once more, is given by

$$\mathcal{A}_{q,N}(f) = \mathcal{A}_{q-1,N}(f) + \Delta \mathcal{A}_{q,N}(f),$$

$$\Delta \mathcal{A}_{q,N}(f) = \sum_{|\mathbf{i}|=q} (\Delta^{i_1} \otimes \dots \otimes \Delta^{i_N}), \tag{35}$$

with $\mathcal{A}_{N-1,N} = 0$ and $q \geq N$. The Eq. (35) can be expanded as

$$\begin{aligned} \mathcal{A}_{q-1,N}(f) &= \sum_{|\mathbf{i}| \leq q-1} (\Delta^{i_1} \otimes \dots \otimes \Delta^{i_N}), \\ \Delta \mathcal{A}_{q,N}(f) &= \sum_{|\mathbf{i}|=q} \sum_{\mathbf{j} \in B_{\mathbf{i}}} (a_{j_1}^{i_1} \otimes \dots \otimes a_{j_N}^{i_N}) \underbrace{(f(Y_{j_1}^{i_1}, \dots, Y_{j_N}^{i_N}) - \mathcal{A}_{q-1,N}(f)(Y_{j_1}^{i_1}, \dots, Y_{j_N}^{i_N}))}_{w_{\mathbf{j}}^i}, \end{aligned} \tag{36}$$

where the new multi-index set reads

$$B_{\mathbf{i}} = \{\mathbf{j} \in \mathbb{N}^N : Y_{j_k}^{i_k} \in X_{\Delta}^{i_k} \text{ for } j_k = 1, \dots, m_{\Delta}^{i_k}, k = 1, \dots, N\}. \tag{37}$$

The hierarchical surplus, $w_{\mathbf{j}}^i$, represents the difference between the function value at a point in the current level of integration and the corresponding value at the previous level. For functions with discontinuities or steep gradients, the magnitude of the surplus grows depending on the strength of the underlying discontinuity. For smooth functions, the hierarchical surplus goes to zero as the interpolation goes to infinity. Thus, the hierarchical surplus is a natural candidate for the sparse grid adaptivity and error control.

As in Ma and Zabarar (2009), we perform the adaptation and refinement process at the level of the single hierarchical basis function (32). This allows us to capture important physical directions of the mechanical concentration tensor (19) and to resolve the singularity of Γ . The basic idea is to use the hierarchical surpluses as an error indicator to detect the smoothness of the solution and refine the hierarchical basis functions $a_{\mathbf{j}}^i$ (32) whose magnitude of the surplus satisfies $w_{\mathbf{j}}^i \geq \hat{\epsilon}$. If this measure is satisfied, we simply add two support nodes for each of the previous integral nodes in each direction. Note that there is a possibility that the same support nodes have already been added by other points, and thus, it is critical to keep track of the uniqueness of the set of active points. For N -dimensional space the number of the active integral nodes, \mathcal{N}_q^a , is

$$\mathcal{N}_q^a \leq 2N \times O(\mathcal{N}_{q-1}^a) \leq (2N)^2 \times O(\mathcal{N}_{q-2}^a) \leq \dots \leq (2N)^q. \tag{38}$$

The implementation details are given in Ma and Zabarar (2009).

3.2. Spherical coordinate system

We recall that the integrand in (19) is a product of the Gamma function and a two-point probability function. Both Γ and S_{rs} have a certain spherical property, i.e., they broadly depend on the distance between two points. Although, the Γ function also carries the directional information and S_{rs} is not always fully isotropic. Nevertheless, we adopt the spherical coordinate system and transform the basis functions, Eq. (32), from Cartesian coordinates $[0,1] \times [0,1] \times [0,1]$ to those in spherical coordinates $[0,R] \times [0,\pi] \times [0,2\pi]$. Fig. 5 shows two basis functions in both coordinate systems. Note that the basis functions are presented in two-dimensions, in the r - θ space, for visualization purpose.

To illustrate the advantages of the integration in spherical coordinates, we consider a test example shown in Fig. 6. The example is a simple integration of a discontinuous density function $\int_0^1 \rho \, d\Omega$, where

$$\rho = \begin{cases} 100 & r \leq 0.3, \\ 1 & r > 0.3. \end{cases} \tag{39}$$

The number of integral points and the integral error for each coordinate system are presented in Table 1. Here the error is calculated as

$$\text{error [\%]} = |I_e^{c,s} - I_n| / |I_e^{c,s}| \times 100, \tag{40}$$

where $I_e^{c,s}$ is the exact analytically calculated integral, and I_n is the numerically evaluated integral, using the sparse grid method (Section 3.1). The superscript c refers to the function integrated in Cartesian coordinates (Fig. 6(a)), and s refers to the function integrated in spherical coordinates (Fig. 6(b)). The surplus tolerance used in this example is $\hat{\epsilon} = 0.001$.

The reduction of integral points is more apparent when the locations of integral points are plotted (Fig. 7). Since the density function has a discontinuity at $r=0.3$, the integral nodes in the Cartesian coordinate system are clustered near the discontinuity and on the projection planes that are consequences of the node generation in the x , y and z directions, respectively. However, the integral nodes in the spherical coordinate system are efficiently organized considering the symmetry of the function.

3.3. Parallel implementation

As we have seen in the previous Section 3.2, the Smolyak integration on the adaptive sparse grid in spherical coordinates is very efficient for functions with spherical character. Despite the adaptivity and the adequacy of the numerical method, it is still numerically expensive, especially when high integral levels are required as in the integration

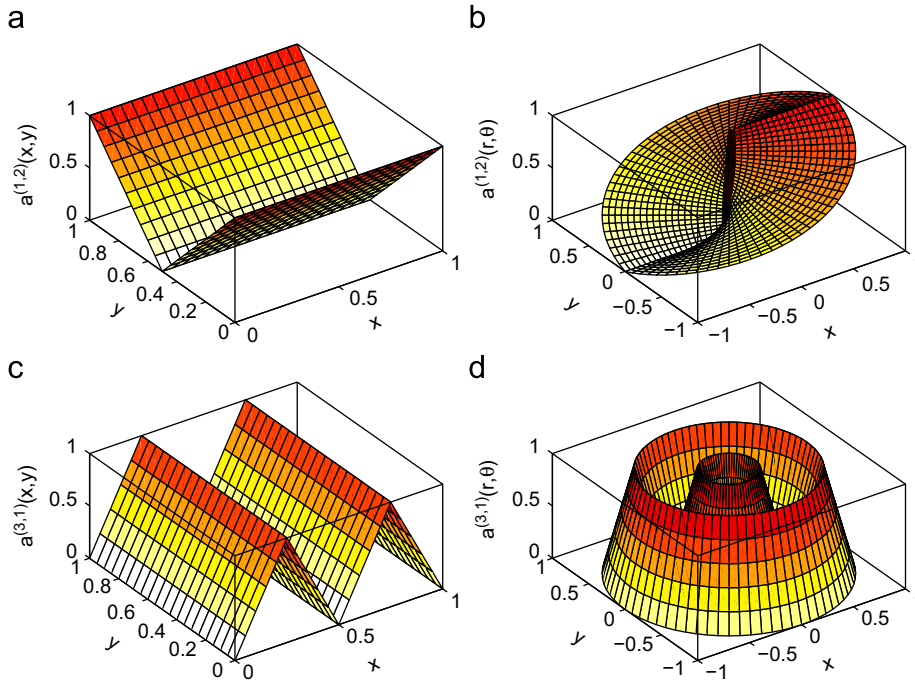


Fig. 5. Comparison of basis functions in Cartesian and polar coordinate systems. Note that the basis functions are presented in two-dimensions for visualization purpose. (a) Cartesian coordinates, $\mathbf{i} = (1,2)$. (b) Polar coordinates, $\mathbf{i} = (1,2)$. (c) Cartesian coordinates, $\mathbf{i} = (3,1)$. (d) Polar coordinates, $\mathbf{i} = (3,1)$.

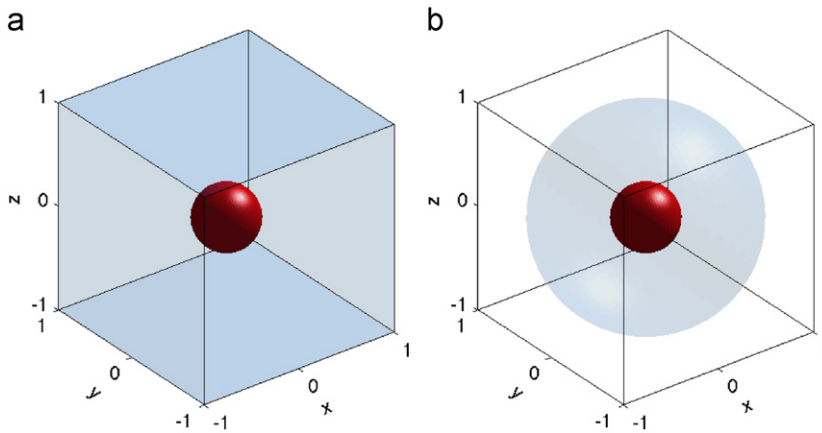


Fig. 6. Density function with discontinuity at $r=0.3$ described by Eq. (39) in Cartesian and spherical coordinates. (a) Function integrated in Cartesian coordinates. (b) Function integrated in spherical coordinates.

Table 1

Comparison between Cartesian and spherical coordinate systems in integrating the discontinuous density function at the same integral level 15. Note the small error and fewer number of points for the spherical integrator.

Coordinates	# Integral nodes	Error (%)
Cartesian	11,409	5.445
Spherical	1261	0.103

of a singular function (Γ). The most expensive parts of the integration algorithm are the routines used to generate new support nodes and to test each support node against all previous active integral nodes to determine if the candidate is active or not. Note that these support nodes are increasing at every hierarchical level as given by Eq. (38) and depicted in Fig. 8.

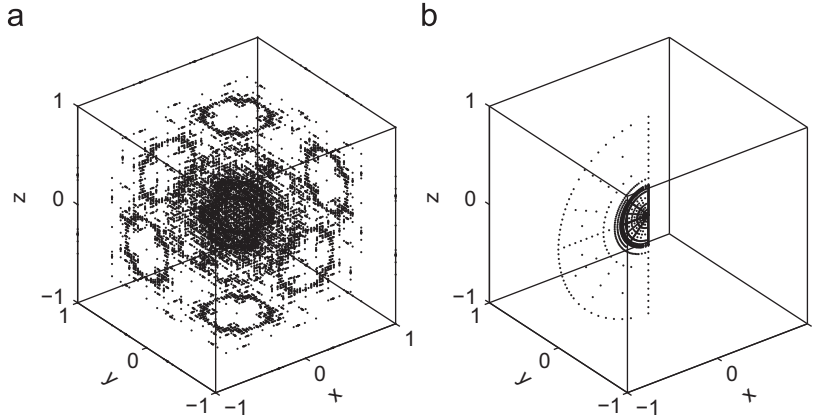


Fig. 7. Distribution of integral nodes in Cartesian and spherical coordinate systems. (a) Cartesian coordinates. (b) Spherical coordinates.

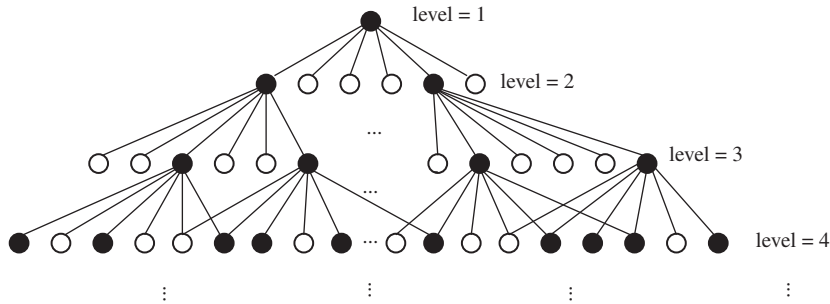


Fig. 8. Integral nodes generation in three-dimensional space. Black nodes are the active nodes. In each new level there are six times more candidate nodes than the number of the active nodes from the previous level.

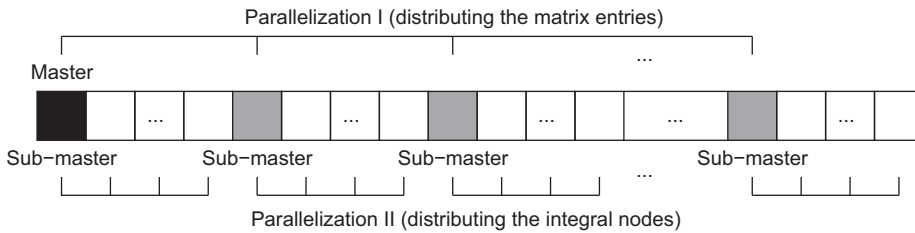


Fig. 9. Double parallelization of computations. (a) Assignment of entries of the mechanical tensor. (b) Distribution of the support nodes.

To optimize the algorithm, we perform the double parallelization depicted schematically in Fig. 9. The first parallel algorithm splits the entries of the mechanical concentration tensor (19). This parallelization strategy is beneficial for fully populated mechanical tensor (full anisotropy) and large n -phase systems. The second parallel algorithm distributes the new integration points across the parallel platform. The second parallelization strategy is useful for all forms of the stiffness tensor. A simple load balancing algorithm that is based on the estimate of the number of searches is provided to keep the work of each processor approximately constant. Once the active nodes are identified, the master processor performs the sorting and removes any duplicate nodes to keep the new active set unique.

The efficacy of the second parallelization strategy, which is the most computationally expensive one, is tested with the formal part of the Gamma function (25). The complexity of the Γ function is shown in Fig. 10. Although it has a very complex structure with a singularity at the origin, the integral of the function is equal to zero (Willis, 1977):

$$\int_{a < |\mathbf{x}| < b} \Gamma \, d\Omega = 0, \quad \forall a \text{ and } b, \text{ with } 0 < a < b. \tag{41}$$

Based on this characteristic, we integrate the Gamma function with $\mu = 3.15$ MPa and $\kappa = 7.92$ MPa from 1.0 to 2.0 μm . The target level of accuracy of the function approximation is selected to be $\hat{\epsilon} = 0.0001$ in this example. Fig. 11(a) shows convergence of the numerical integral. The parallel efficiency of our method is shown in Fig. 11(b). The speedup is obtained for a fixed integration level $q=23$ with 622,971 number of integral points. Almost 68% parallel efficiency is achieved for

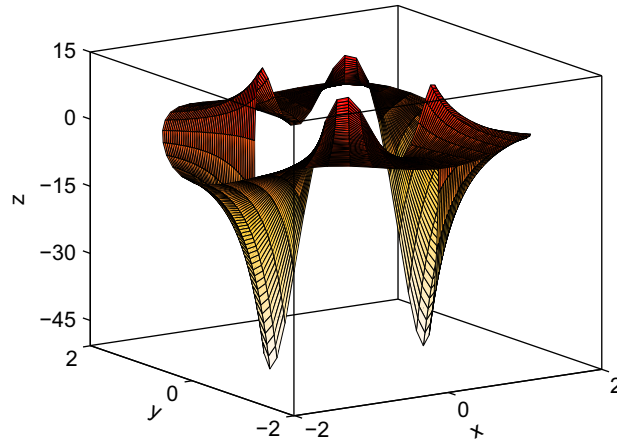


Fig. 10. Two-dimensional representation of the Γ_{1111} component in the interval $1 \leq x \leq 2$ and $1 \leq y \leq 2$ microns.

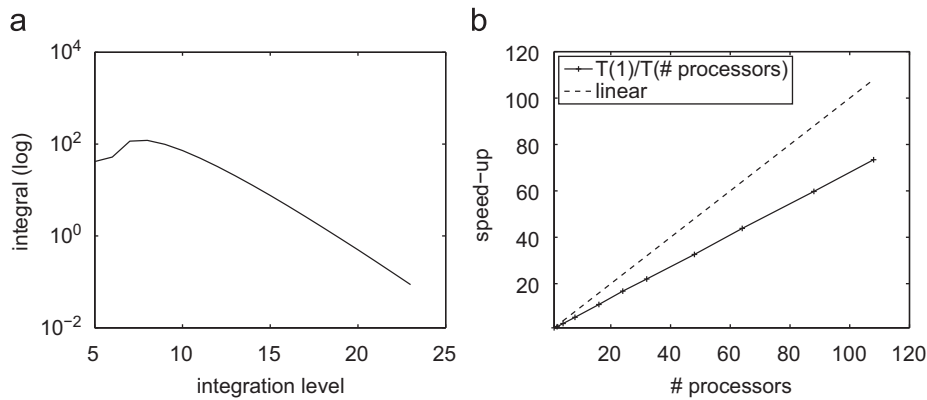


Fig. 11. (a) Evolution of the integral (41) as a function of the integration level. (b) Parallel scalability of the adaptive sparse integration scheme for problem (41).

the current implementation. We attribute this deviation from a perfectly scalable algorithm to several local searches required to create a unique set of active points. A more sophisticated implementation using a hash table, for example, is required to improve the parallel performance.

4. Numerical examples

In this section, we present three examples to demonstrate the physical observations that are captured due to new numerics used in this work. This improved numerical scheme allows us to efficiently capture the anisotropic, three-dimensional response using real micro-CT generated probability spectrum. The first example is devoted to both model verification and validation. The second example is focused on a lattice type system in order to demonstrate the anisotropy and to confirm that proper symmetries typical for lattice structures are obtained. The last example is devoted to computing properties of particulate systems with the real material statistics that are obtained using microtomography. Details on micro-CT analysis and evaluation of a probability spectrum have been reported in Lee et al. (2009). We use isotropic constituents and an orthotropic overall material response in our examples, with six independent material constants ($\bar{E}_x, \bar{E}_y, \bar{E}_z, \bar{G}_{xy}, \bar{G}_{xz}, \bar{G}_{yz}$). However, our solver is general and can compute overall properties of fully anisotropic medium with 21 independent constants. All examples are computed on 128 CPUs using only the parallelization II strategy.

4.1. Polydisperse particulate material—model validation

In this section, we focus on model verification and validation. An experimental data set from the work of Smith (1976) is used for validation. A heterogeneous composite studied in Smith (1976) consists of glass beads embedded in an epoxy matrix. Thus, the material system is considered to be a two-phase composite, with isotropic particles p and an isotropic matrix m . The mechanical properties of these particles are, $E_p = 76.0$ GPa and $\nu_p = 0.23$, whereas those of the matrix are, $E_m = 3.0$ GPa and $\nu_m = 0.4$. Perfect bonding between particles and a matrix is assumed in this study.

The distribution of the particle diameters is not exactly described in Smith (1976), but it is reported that it is in the range of 1–30 μm . Therefore, we use a normal distribution for the diameter of particles, in this range, and generate simulated packs using *Rocpack*, a particle packing software (Maggi et al., 2008). To compare our result with the experimental data, five different volume fractions (c_p) are considered: 0.100, 0.202, 0.302, 0.401, and 0.499. Fig. 12 shows one packing realization with a volume fraction of $c_p=0.499$. The corresponding distribution of the particle sizes, for this pack, is depicted in Fig. 13.

We would like to investigate the effect of the pack statistics on the anisotropy of elastic constants. Thus, we consider both the complete, $S_{rs}(\mathbf{x}-\mathbf{x}')$, and the isotropic, $S_{rs}(|\mathbf{x}-\mathbf{x}'|)$, probability spectrum. Fig. 14 shows a complete two-point

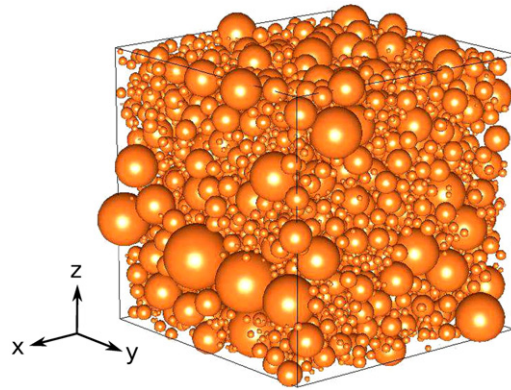


Fig. 12. Polydisperse pack with $c_p=0.499$ volume fraction generated by *Rocpack*. The size of the pack is $241.03 \mu\text{m} \times 241.03 \mu\text{m} \times 241.03 \mu\text{m}$. This pack consists of 5002 particles.

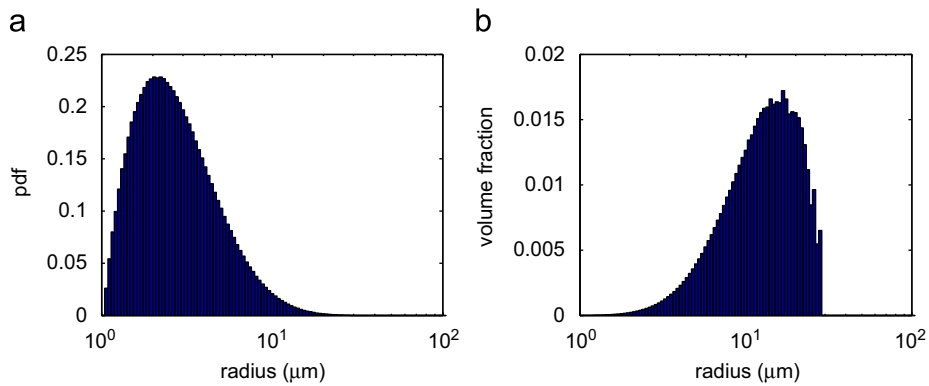


Fig. 13. Distribution of the particle diameter for the pack shown in Fig. 12. (a) Pdf of particle diameters. (b) Volume fraction of particle diameters.

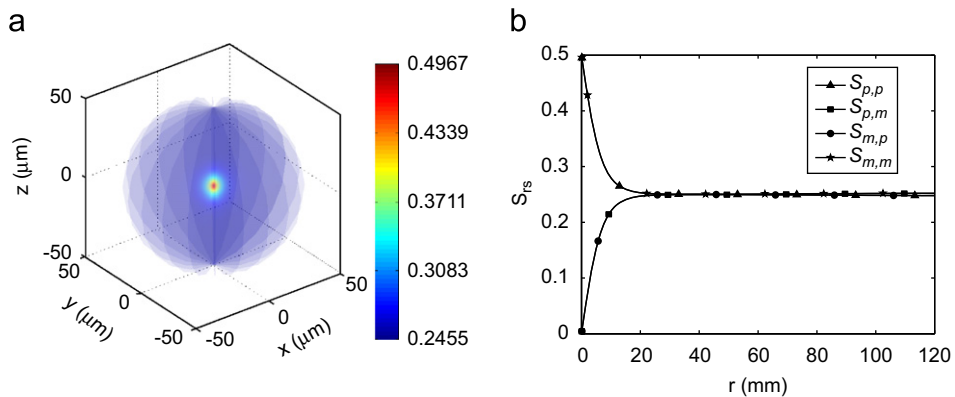


Fig. 14. Two-point probability functions computed for the pack shown in Fig. 12. Sampling procedure is described in Lee et al. (2009). We use 200,000 throws of a sampling template with 1000 radial points and 20 circumferential points in this example. (a) Complete S_{mm} . (b) Isotropic two-point probability functions.

probability function, S_{mm} , and the isotropic two-point probability functions computed for the pack depicted in Fig. 12. The isotropic two-point probability functions are obtained by averaging the complete two-point probability functions over all possible directions. The maximum standard deviation that represents the variation from the perfect statistical isotropy is $\hat{\sigma}_{mm} = 0.004$. The second-order probability functions also provide the characteristic material length scale, i.e., the length for which two material points become statistically independent. We use the characteristic material length scale to reduce the size of the integration domain, when we compute the mechanical concentration tensor \mathcal{A}_{rs} (Eq. (19)). In this example, we integrate the domain bounded by the radius of 50 μm , rather than the entire domain since the rest of the domain does not statistically influence the results. This approach has been confirmed by studying the size of the integration window.

For the perfectly statistically isotropic medium, the integral that appears in (19) leads to

$$\int_{\Omega_{\mathbf{x}'}} \Gamma(\mathbf{x}-\mathbf{x}')(S_{rs}(\mathbf{x}-\mathbf{x}')-c_r c_s) d\Omega_{\mathbf{x}'} = \mathbf{P}[S_{rs}(\mathbf{0})-c_r c_s], \tag{42}$$

where

$$\mathbf{P} = \int_{|\mathbf{x}'| < a} \Gamma d\Omega \equiv \Gamma^s \quad \forall a > 0, \tag{43}$$

as pointed out in Willis (1977) and Buryachenko (2007). We take advantage of this fact and assess the error due to our numerical integration using the characteristic in (41) and (43). Moreover, one can set $\mathbf{P}_0 = \Gamma_0^s$ by substituting $\mu = \mu_0$ and $\kappa = \kappa_0$ in (23), where μ_0 and κ_0 are the shear and bulk moduli of a comparison medium, respectively.

Since the Γ function is singular at the origin, we do not integrate the singularity exactly and approximate the integral (42) by

$$\int_{\Omega_{\mathbf{x}'}} \Gamma(\mathbf{x}-\mathbf{x}')(S_{rs}(\mathbf{x}-\mathbf{x}')-c_r c_s) d\Omega_{\mathbf{x}'} \approx \int_{\Omega_{\mathbf{x}'}\setminus\nu} \Gamma(\mathbf{x}-\mathbf{x}')(S_{rs}(\mathbf{x}-\mathbf{x}')-c_r c_s) d\Omega_{\mathbf{x}'}, \tag{44}$$

where ν is the small volume close to the singularity that we remove. In our examples, this volume ν is characterized by the distance $\hat{\varepsilon}$ from the origin. Furthermore, we replace the exact integral $\int_{\Omega_{\mathbf{x}'}} \bullet d\Omega_{\mathbf{x}'}$ by the numerical integral $\mathcal{I}_{q,N}(\bullet|\Omega_{\mathbf{x}'}\setminus\nu)$ using the sparse Smolyak algorithm presented in Section 3.1. Therefore, our numerical accuracy depends on three parameters, namely the quality of the interpolation $\hat{\varepsilon}$, the quality of the singular integration $\tilde{\varepsilon}$ and on the convergence of the integral that is controlled by the integral level q . We will comment on these numerical tolerances hereafter. To better understand all of the influences discussed above, three models are defined as

$$\begin{aligned} &\text{singular model} - \mathbf{P}_0[S_{rs}(\mathbf{0})-c_r c_s], \\ &\text{isotropic model} - \int_{\Omega_{\mathbf{x}'}} \Gamma_0(\mathbf{x}-\mathbf{x}')(S_{rs}(|\mathbf{x}-\mathbf{x}'|)-c_r c_s) d\Omega_{\mathbf{x}'}, \\ &\text{anisotropic model} - \int_{\Omega_{\mathbf{x}'}} \Gamma_0(\mathbf{x}-\mathbf{x}')(S_{rs}(\mathbf{x}-\mathbf{x}')-c_r c_s) d\Omega_{\mathbf{x}'}. \end{aligned} \tag{45}$$

Note that the singular model leads to a closed-form formula for $\bar{\mathbf{L}}$

$$\bar{\mathbf{L}} = \sum_{r=1}^N c_r \mathbf{L}_r [\mathbf{I} + \mathbf{P}_0(\mathbf{L}_r - \mathbf{L}_0)]^{-1} \left\{ \sum_{s=1}^N c_s [\mathbf{I} + \mathbf{P}_0(\mathbf{L}_s - \mathbf{L}_0)]^{-1} \right\}^{-1}, \tag{46}$$

where \mathbf{I} is the identity matrix, and \mathbf{P}_0 is given by Eq. (43). The formula (46) was given in Willis (1977). The singular and isotropic models are compared for the purpose of verification as these should lead to the same result. This verification is performed for all examples presented in this work.

To quantify the anisotropic response of the glass-bead composite, we introduce a mean macroscopic Young's modulus

$$\bar{E}^{i,a} = (\bar{E}_x^{i,a} + \bar{E}_y^{i,a} + \bar{E}_z^{i,a})/3. \tag{47}$$

where \bar{E}^i denotes the overall modulus from the isotropic model, whereas \bar{E}^a represents the mean modulus computed by the anisotropic model (We assume an orthotropic overall material behavior in our work). For the singular model, all principal directions are identical, and we simply set $\bar{E}^s = \bar{E}_x$. Fig. 15 shows the comparison of the overall Young's modulus for the singular model, statistically isotropic model and the model with fully resolved probability spectrum, anisotropic model, that leads to a certain degree of anisotropy. Experimental data from Smith (1976) is also included. As expected for this example, all models coincide due to the high isotropy of the pack. All computations are performed with the matrix m serving as the comparison medium in this example (lower bound).

The quality of the interpolation is controlled with $\hat{\varepsilon} = 0.0005$ and the singular integration is attained with $\tilde{\varepsilon} = 0.1 \mu\text{m}$. All solutions are stopped when the integral converges within a certain tolerance,

$$\mathcal{E}_{\mathcal{I}} = |\mathcal{I}_q - \mathcal{I}_{q-1}| / |\mathcal{I}_{q-1}| \leq \text{tol}_1, \tag{48}$$

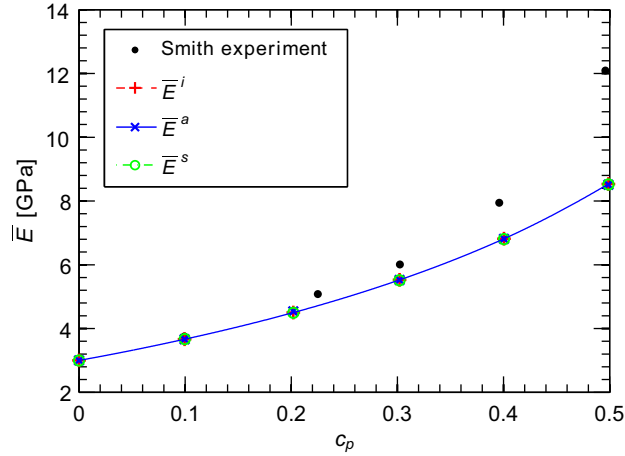


Fig. 15. Comparison of overall Young's modulus, \bar{E} , between experimental data and the isotropic and the anisotropic numerical results. The singular model solution, \bar{E}^s , is also included for verification. Due to the low anisotropy of the packs, the overall Young's modulus is identical (in numerical sense) for all numerical schemes, which verifies the model.

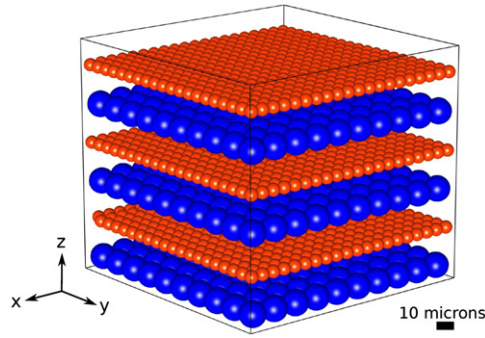


Fig. 16. Bimodal lattice pack containing 1200 small and 300 big particles.

or when the maximum surplus, w_j^i , normalized by the maximum amplitude of the function over the integral domain is within a given tolerance

$$\mathcal{E}_{\mathcal{M}} = \frac{\max_j w_j^i}{\mathcal{A}_q(f_{max}) - \mathcal{A}_q(f_{min})} \leq tol_2 \quad \text{at } |\mathbf{i}| = q. \tag{49}$$

The integration stops, if one of these criteria is smaller than a corresponding threshold for two consecutive levels of the interpolation/integration. The second stopping criterion is introduced to eliminate the numerical pollution that can develop for large integral domains. The function values given by (45) oscillate around zero far away from the origin, because $S_{rs}(|\mathbf{x}-\mathbf{x}'|) \rightarrow c_r c_s$ as $|\mathbf{x}-\mathbf{x}'| \rightarrow \infty$. Therefore, large numerical errors can be accumulated even when w_j^i approaches zero for large $\Omega_{\mathbf{x}} \setminus v$. In this first example, we set $tol_1 = tol_2 = 0.005$. To quantify the precision, or numerical error, the variation within the directional components of the mechanical properties is compared. The numerical error of the isotropic model is defined as

$$e_n = (\max(\bar{E}_x^i, \bar{E}_y^i, \bar{E}_z^i) - \min(\bar{E}_x^i, \bar{E}_y^i, \bar{E}_z^i)) / \bar{E}^i \times 100 \%. \tag{50}$$

For the volume fraction equal to 0.499, $e_n = 0.08\%$ and the isotropic model deviates from the singular one by 0.15% (Willis' model (Eq. (46))). This verifies our model. The elastic modulus calculated from the anisotropic model deviates by 0.27% from the isotropic approximation. Note again that the standard deviation from perfect statistical isotropy was $\hat{\sigma}_{mm} = 0.004$. Therefore, it is not surprising that the anisotropic model does not deviate much from the isotropic one. This is not the case in general as will be shown hereafter.

4.2. Lattice pack

To investigate the anisotropy of the material, we study the periodic lattice pack (Fig. 16) that is anisotropic (transverse isotropic). The bimodal lattice pack is composed of small and large beads. Small particles with packing fraction of 0.087

are 5 μm in diameter and large particles with packing fraction of 0.174 are 10 μm in diameter. The total pack dimensions are $100 \times 100 \times 90 \mu\text{m}^3$ with the total particle volume fraction of 0.261.

Fig. 17 shows the complete S_{mm} probability function, $S_{rs}(\mathbf{x}-\mathbf{x}')$, and selected isotropic, $S_{rs}(|\mathbf{x}-\mathbf{x}'|)$, two-point probability functions. As can be observed, the matrix–matrix probability function is not isotropic and captures the layered nature of the pack morphology with bands of lower and higher probability of realization. Note that for the multi-layered pack, the probability functions do not saturate, as in Fig. 14(b), but rather oscillate with the period of the microstructure (layers) as seen in Fig. 17(b). This is a consequence of the long-range order (Torquato, 2002). Note that all nine second-order probability functions are evaluated for this three-phase medium. The comparison medium \mathbf{L}_0 is set in this example as $\mathbf{L}_0 = c_1 \mathbf{L}_1 + c_2 \mathbf{L}_2 + c_m \mathbf{L}_m$, where c_1 , c_2 , and c_m are the volume fractions of big particles, small particles, and the matrix, respectively. The properties of individual constituents are listed in Table 2. The overall mechanical properties are computed by the singular, isotropic and anisotropic models in order to assess the effect of the statistical information on the anisotropic mechanical properties. The interpolation is controlled by $\hat{\epsilon} = 0.0002$, and the singular integration is governed by $\tilde{\epsilon} = 0.1$, in this example. The error of the integration is controlled by (48) and (49) with $\mathcal{E}_I = \mathcal{E}_M \leq 0.005$. The size of the integration window is 50 μm . Due to the quick decay of the Γ function, the window size of 50 μm is sufficient in this example as has been verified by the convergence study.

Using Eq. (47), the isotropic model predicts $\bar{E}^i = 46.418$ GPa with a numerical error of $e_n = 0.373\%$, as defined by Eq. (50). The isotropic model should produce equivalent results to the singular model (verification), which yields $\bar{E}^s = 46.379$ GPa. \bar{E}^i differs from \bar{E}^s by 0.084%. The mean shear modulus yields $\bar{G}^i = 17.640$ GPa with a numerical error $e_n = 0.886\%$, and this modulus deviates by 1.21% from the singular model that predicts $\bar{G}^s = 17.857$ GPa. Note that numerical error in the shear modulus is computed in the same fashion as for Young’s modulus by proper exchange of variables in Eq. (50). The anisotropic results are listed in Table 3. The lattice has a symmetric structure in the x and y directions (transverse isotropy). Therefore, \bar{E}_x and \bar{E}_y constants are similar (deviation is due to the numerical error). Moreover, the x – y properties are stiffer, because the lattice is densely packed in that direction, whereas a more compliant

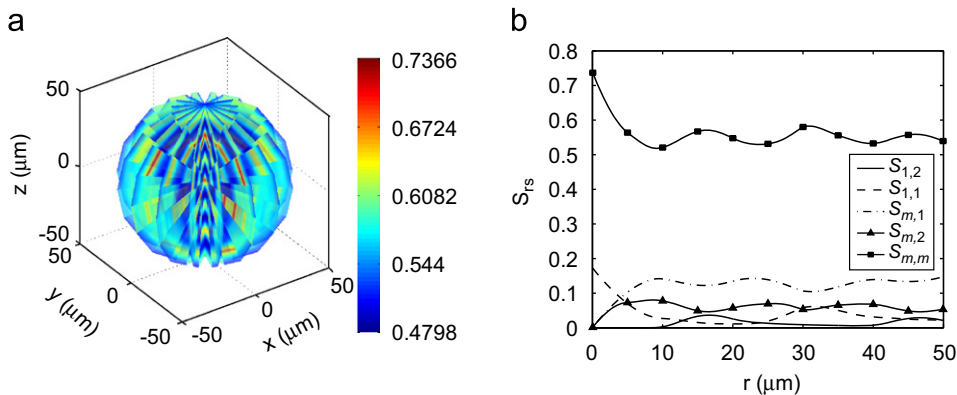


Fig. 17. Two-point probability functions computed for lattice pack shown in Fig. 16. We use 2,000,000 throws of a sampling template with 1000 radial points and 64 circumferential points in this example. Note that the functions are continuous and periodic, and the patch-like character in (a) is a visualization artifact. (a) Complete S_{mm} . (b) Isotropic two-point probability functions.

Table 2
Volume fraction, Young’s modulus (E) and Poisson’s ratio (ν) for lattice pack constituents. Note that constituents are assumed isotropic.

Phase	Volume fraction	E (GPa)	ν
Big-1	0.174	3	0.4
Small-2	0.087	120	0.34
Matrix-m	0.740	60	0.2

Table 3
Overall properties in (GPa) for the lattice pack shown in Fig. 16 computed by the anisotropic model.

\bar{E}_x	\bar{E}_y	\bar{E}_z	\bar{G}_{xy}	\bar{G}_{yz}	\bar{G}_{zx}
51.976	52.783	43.797	19.302	14.861	14.852

modulus \bar{E}_z is obtained in the z direction. The difference between x – y and x – z or y – z properties yields $(\bar{E}_x + \bar{E}_y)/2 - \bar{E}_z = 8.58$ GPa, which constitutes a 16.38% difference (anisotropy). Shear behavior of the homogenized continuum is more isotropic since shear planes can develop in both x – y and x – z or y – z directions, respectively. The weakest material, the large beads, are favorably oriented for x – y slip, but their volume fraction is relatively low and the matrix increases the overall shear modulus. The x – z and y – z slip planes cut across the stiffest material, but the thickness of the small particles is small, and thus, the shear modulus does not deviate from the mean dramatically.

4.3. Polydisperse pack with two dominant modes

In the last example, we focus on computing the mechanical properties of a heterogeneous system that is characterized using microtomography. A sample pack is composed of spherical glass beads with average diameters of 44 and 250 μm in a 3.175 mm diameter scanning tube (Fig. 18). The details on sample preparation, the scanning procedure and computation of statistics are given in our previous work (Lee et al., 2009). The image processing is done in *Amira* (Visage Imaging Inc.). The resolution for this scan is 4.638 μm per voxel. To compute the statistics of the material, we acquire a block ($1477.14 \times 1538.96 \times 2645.00 \mu\text{m}^3$) from the core of the 3D scanned image in Fig. 18. That corresponds to 60.3 million voxels. There are 48,214 small particles and 163 big particles with volume fractions $c_1 = 0.402$ (small particles) and $c_2 = 0.207$ (big particles) in the composite. Fig. 19 shows detected particles and the position of the big particles in particular. Note that the big particles are clustered on one side of the pack, which indicates the anisotropy of the pack.

As in the previous examples, we consider two types of the two-point probability functions, i.e., the complete probabilities, $S_{rs}(\mathbf{x}-\mathbf{x}')$, and the isotropic ones, $S_{rs}(|\mathbf{x}-\mathbf{x}'|)$ (Fig. 20). For the three-phase composite considered in this example, we compute nine second-order probability functions. Fig. 20(b) shows the complexity of S_{1m} close to the origin that is associated with small particles, and the long-range structure of S_{22} related to the mean diameter of large particles (250 μm). The S_{mm} is also complex in the $\sim 44 \mu\text{m}$ range (the mean diameter of small particles) since it highly depends on morphology or reinforcement. All of these statistical features directly impact the mechanical properties, and their proper integration in (19) is essential. The results from the isotropic model are used to measure the numerical error. The quality of interpolation is dictated by $\hat{\varepsilon} = 0.0001$, and the singular integration is set as $\tilde{\varepsilon} = 0.1$, in this example. The error of integration is controlled by (48) and (49) with $\mathcal{E}_T = \mathcal{E}_M \leq 0.001$, and the size of the integration window is 500 μm . The size of the integration window was verified by a convergence study once more. To study different scenarios relevant in analysis of multi-phase continuum, we analyze two three-phase composite mixtures with small particles, big particles and a matrix. The two formulations have the same microstructure and differ only in the mechanical properties of the constituents. Table 4 shows the mechanical properties of individual constituents for both formulations. The comparison medium for this example is, $\mathbf{L}_0 = c_1 \mathbf{L}_1 + c_2 \mathbf{L}_2 + c_m \mathbf{L}_m$.

The mechanical properties of the first formulation computed using the isotropic model are, $\bar{E}^i = 31.829$ GPa and $\bar{G}^i = 10.825$ GPa with normal $e_n = 0.157\%$ and shear $e_n = 1.460\%$ numerical errors, respectively. The singular model used for verification yields $\bar{E}^s = 31.869$ GPa and $\bar{G}^s = 11.153$ GPa with normal 0.126% and shear 2.94% verification errors. The isotropic properties of the second formulation are $\bar{E}^i = 56.882$ GPa and $\bar{G}^i = 20.605$ GPa. The numerical errors are $e_n = 0.154\%$ (normal) and $e_n = 1.170\%$ (shear). The singular model used for verification yields $\bar{E}^s = 57.441$ GPa and $\bar{G}^s = 20.969$ GPa, and the errors with respect to the isotropic model are 0.973% and 1.74%. All errors are evaluated as in the previous examples. Note that these errors are small considering the size of the integral domain and complexity of probability space. The mechanical properties computed with the anisotropic model are listed in Table 5. To evaluate the

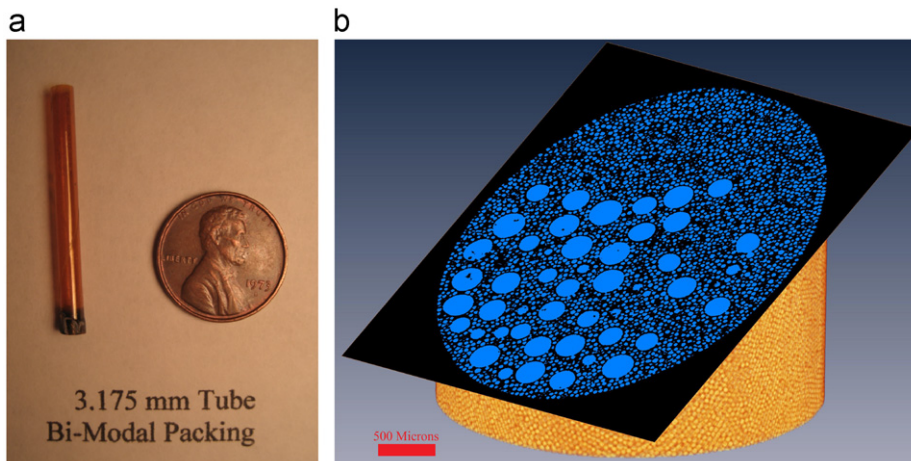


Fig. 18. Polydisperse glass beads system. The pack has two dominant modes of 44 μm and 250 μm . (a) Specimen. (b) Tomographic scan.

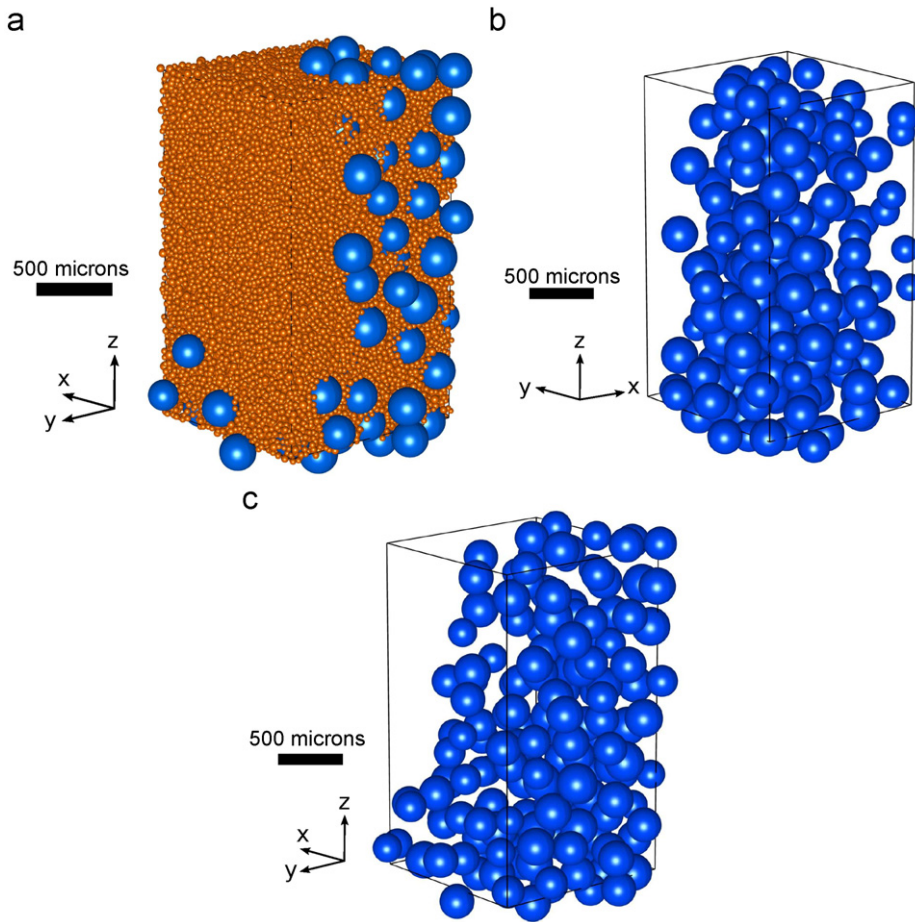


Fig. 19. (a) Location of particles in the pack. There are 48,214 small and 163 big particles in the pack. (b) and (c) show different views of the large particles in the pack.

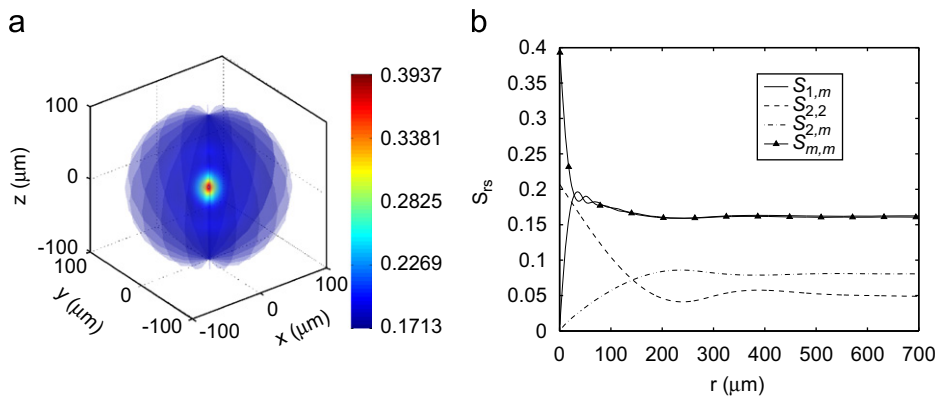


Fig. 20. Two-point probability functions of the polydisperse tomographically characterized pack. Note the very complex shape of the probability functions close to the origin. We use 1,000,000 throws of a sampling template with 1000 radial points and 20 circumferential points in this example. Only selected second-order probability functions are plotted. (a) Complete S_{mm} . (b) Isotropic two-point probability functions.

extent of the anisotropy the following measure is introduced,

$$\mathcal{M}_A[\%] = \max(|\bar{E}_x - \bar{E}^i|, |\bar{E}_y - \bar{E}^i|, |\bar{E}_z - \bar{E}^i|) / \bar{E}^i \times 100. \tag{51}$$

The first formulation shows anisotropy in the x and z directions with $\mathcal{M}_A = 5.209\%$. Recall that the biggest particles are the stiffest ones in this case. It can be observed, Fig. 19, that big particles are diluted in the x – y plane, but they form

Table 4
Mechanical properties of individual isotropic phases for two formulations. Young’s modulus E is in (GPa).

	Matrix	Small particles	Big particles
Formulation 1	$E=3.0, \nu=0.40$	$E=60.0, \nu=0.20$	$E=120.0, \nu=0.34$
Formulation 2	$E=120.0, \nu=0.34$	$E=60.0, \nu=0.20$	$E=3.0, \nu=0.40$

Table 5
Overall properties in (GPa) for the pack in Fig. 19 computed by the anisotropic model.

Formulation	\bar{E}_x	\bar{E}_y	\bar{E}_z	\bar{G}_{xy}	\bar{G}_{yz}	\bar{G}_{zx}
1	33.487	32.392	33.254	10.317	11.330	11.208
2	54.519	56.658	59.862	20.047	21.549	21.515

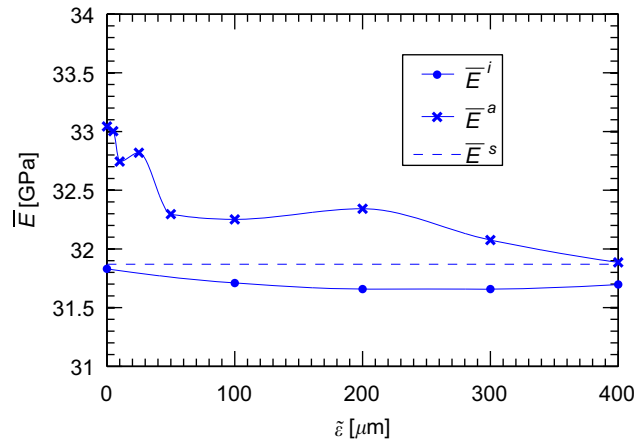


Fig. 21. Effect of the singularity on the numerical integration for polydisperse glass bead system with formulation 1. $\tilde{\epsilon} \in (0.1; 400)$.

a dominant column-like structure in the z direction, which coincides with the longitudinal axis of the straw. Moreover, the column is spreading more toward the x direction in the x – y plane at the base. This column is created due to the improper mixing and pouring of glass beads into a straw, which produces this directional anisotropy. The shear anisotropy for the first formulation, measured with the same formula appropriately modified for \bar{G} , is $\mathcal{M}_A = 7.352\%$. Once more, the column-like structure that developed stiffens more both \bar{G}_{yz} and \bar{G}_{zx} moduli, whereas \bar{G}_{xy} is the weakest one, since the matrix has the lowest shear modulus and favorable slip planes can develop in the x – y plane with the smallest number of big particles to be intersected. Formulation 2 also has the stiffest response in the z direction with the anisotropic measure reaching $\mathcal{M}_A = 5.239\%$. Note that we use the same formula to construct the comparison medium, which leads to different elastic constants of the comparison medium for formulation 2. Although big particles are the softest ones in this case, their concentration and distribution does not alter the response in the z direction substantially. It is interesting to observe from Fig. 19 that large particles are positioned diagonally in the x – y plane with moderate preference in the x direction. Thus, a similar response in these directions, weighted by the stiffer ($\bar{E}_x > \bar{E}_y$, formulation 1) or by the softer ($\bar{E}_x < \bar{E}_y$, formulation 2) large particles, can be expected and is correctly predicted for both formulations.

We are also interested in the effect of the singular integration parameter, $\tilde{\epsilon}$, on the elastic properties. Fig. 21 shows the effective modulus of formulation 1, \bar{E} , as a function of $\tilde{\epsilon}$. The singular model (Eq. (46)) is shown by the horizontal dashed line. It can be seen that the isotropic model is almost unaffected by the size of the singular exclusion and is within 1% of the singular model. Exact integration would lead to a flat line, and thus, the deviation can be viewed as a numerical error. These errors are consequences of both the integration and statistical sampling methods. The numerical error for the isotropic model when $\tilde{\epsilon} = 0.1$ is $e_n = 0.157\%$. On the other hand, the anisotropic model shows marked sensitivity to Γ (singularity) and $S_{\mathbb{R}}(\mathbf{x} - \mathbf{x}')$ structure. Notice that the changes in \bar{E}^a occur close to the singularity, the mean diameter of the small glass beads, and the mean diameter of the large glass beads (44 and 250 μm , see Fig. 20(b) for structure of $S_{\mathbb{R}}(|\mathbf{x} - \mathbf{x}'|)$).

5. Conclusions

In this manuscript, we propose a computational scheme for evaluation of mechanical properties of polydisperse particulate composites. The complex statistical characteristics are obtained from micro-CT data. The well-known Hashin–Shtrikman–Willis

variational principle, that links directly the statistical descriptors to mechanical properties, is adopted. Unfortunately, computation of mechanical tensors that are building blocks of the Hashin–Shtrikman–Willis model is very demanding. To alleviate this problem, we employ the adaptive sparse Smolyak integration method with hierarchical basis. Moreover, we extend it to spherical coordinates and parallelize it for our particular problem. We show that spatially complex mechanical tensors, based on fully resolved anisotropic probability spectrum, can be efficiently integrated. Due to our improved numerics, we capture in detail the anisotropic response of polydisperse particulate packs that is often hidden. We validate our numerical method by comparing computer-generated packs to experimental data, and verify the isotropic model against a closed-form expression. Finally, we apply the method to a real polydisperse system that is obtained using microtomography.

Future research directions are to compute both bounds and to extend this technique to nonlinear media. Application to ellipsoidal packs and/or other crystalline shapes, where anisotropy is more pronounced, needs to be investigated. The third-order model with realistic tomographically characterized probability descriptors that will tighten the bounds is also of interest.

Acknowledgments

The authors would like to acknowledge the support from Buckmaster Research—DoD STTR program, AFOSR: Dr. J. Buckmaster (Buckmaster Research) and Dr. A. Nachman (AFOSR) program managers.

References

- Arns, C.H., Knackstedt, M.A., Mecke, K.R., 2003. Reconstructing complex materials via effective grain shapes. *Physical Review Letters* 91 (21) 215506–1–215506–4.
- Arns, C.H., Knackstedt, M.A., Pinczewski, W.V., 2002. Computation of linear elastic properties from microtomographic images: methodology and agreement between theory and experiment. *Geophysics* 67 (5), 1396–1405.
- Bensoussan, A., Lions, J.L., Papanicolaou, G., 1978. *Asymptotic Analysis for Periodic Structures*. North-Holland, New York.
- Beran, M.J., 1968. *Statistical Continuum Theories*. Interscience Publishers.
- Bernal, J.D., 1959. A geometric approach to the structure of liquids. *Nature* 183, 141–147.
- Bouvard, D., Chaix, J.M., Dendievel, R., Fazekas, A., Ltang, J.M., Peix, G., Quenard, D., 2007. Characterization and simulation of microstructure and properties of eps lightweight concrete. *Cement and Concrete Research* 37, 1666–1673.
- Bungartz, H.J., Griebel, M., 2004. Sparse grids. *Acta Numerica* 13, 147–269.
- Buryachenko, V.A., 2007. *Micromechanics of Heterogeneous Materials*. Springer.
- Castaneda, P.P., 1998. Three-point bounds and other estimates for strongly nonlinear composites. *Physical Review B* 57 (19), 12077–12083.
- Christensen, R.N., Lo, K.H., 1979. Solutions for effective properties of composite materials. *Journal of the Mechanics and Physics of Solids* 27, 315–330.
- Drugan, W.J., 2003. Two exact micromechanics-based nonlocal constitutive equations for random linear elastic composite materials. *Journal of the Mechanics and Physics of Solids* 51, 1745–1772.
- Drugan, W.J., Willis, J.R., 1996. A micromechanics-based nonlocal constitutive equation and estimates of representative volume element size for elastic composites. *Journal of the Mechanics and Physics of Solids* 44 (4), 492–524.
- Rolland du Roscoat, S., Decain, M., Thibault, X., Geindreau, C., Bloch, J.-F., 2007. Estimation of microstructural properties from synchrotron X-ray microtomography and determination of the r_{ve} in paper materials. *Acta Materialia* 55, 2841–2850.
- Dvorak, G.J., Srinivas, M.V., 1999. New estimates of overall properties of heterogeneous solids. *Journal of the Mechanics and Physics of Solids* 47, 899–920.
- Eshelby, J.D., 1957. The determination of the elastic field of an ellipsoidal inclusion, and related problems. *Proceedings of the Royal Society of London. Series A, Mathematical and Physical* 241 (1226), 376–396.
- Fokins, A.G., Shermegor, T.D., 1969. Calculation of effective elastic moduli of composite materials with multiphase interactions taken into consideration. *Zhurnal Prikladnoi Mekhaniki i Tekhnicheskoi Fiziki* 10 (1), 51–57.
- Fullwood, D.T., Adams, B.L., Kalidindi, S.R., 2008. A strong contrast homogenization formulation for multi-phase anisotropic materials. *Journal of the Mechanics and Physics of Solids* 56, 2287–2297.
- Gallier, S., Hiernard, F., 2008. Microstructure of composite propellants using simulated packings and X-ray tomography. *Journal of Propulsion and Power* 24 (1), 147–150.
- Gerstner, T., Griebel, M., 1998. Numerical integration using sparse grids. *Numerical Algorithms* 18, 209–232.
- Hashin, Z., Shtrikman, S., 1962. On some variational principles in anisotropic and nonhomogeneous elasticity. *Journal of the Mechanics and Physics of Solids* 10, 335–342.
- Hill, R., 1985. On the micro-to-macro transition in constitutive analyses of elastoplastic response at finite strain. *Mathematical Proceedings of the Cambridge Philosophical Society* 98, 579–590.
- Lee, H., Brandyberry, M., Tudor, A., Matouš, K., 2009. Three-dimensional reconstruction of statistically optimal unit cells of polydisperse particulate composites from microtomography. *Physical Review E* 80 (6) 061301–1–061301–12.
- Ma, X., Zabarar, N., 2009. An adaptive hierarchical sparse grid collocation algorithm for the solution of stochastic differential equations. *Journal of Computational Physics* 228, 3084–3113.
- Maggi, F., Stafford, S., Jackson, T.L., Buckmaster, J., 2008. Nature of packs used in propellant modeling. *Physical Review E* 77 (046107) 046107–1–046107–17.
- Matouš, K., 2003. Damage evolution in particulate composite materials. *International Journal of Solids and Structures* 40 (6), 1489–1503.
- Matteo, F., Johnson, S.G., 2005. The design and implementation of FFTW3. *Proceedings of the IEEE* 93 (2), 216–231 Special issue on “Program Generation, Optimization, and Platform Adaptation”.
- Prochazka, P.P., Šejnoha, J., 2004. Extended Hashin–Shtrikman variational principles. *Applications of Mathematics* 49 (4), 357–372.
- Ranganathan, S.I., Ostoja-Starzewski, M., 2008. Scaling function, anisotropy and the size of rve in elastic random polycrystals. *Journal of the Mechanics and Physics of Solids* 56, 2773–2791.
- Smith, J.C., 1976. Experimental values for the elastic constants of a particulate-filled glassy polymer. *Journal of Research of the National Bureau of Standards—A Physics and Chemistry* 80A, 45–49.
- Smolyak, S., 1963. Quadrature and interpolation formulas for tensor product of certain classes of functions. *Soviet Mathematics Doklady* 4, 240–243.
- Talbot, D.R.S., Willis, J.R., 1985. Variational principles for inhomogeneous nonlinear media. *IMP Journal of Applied Mathematics* 35, 39–54.
- Torquato, S., 1987. Thermal conductivity of disordered heterogeneous media from the microstructure. *Reviews in Chemical Engineering* 4 (3&4), 151–204.
- Torquato, S., 1997. Exact expansion for the effective elastic tensor of disordered composites. *Physical Review Letters* 79 (4), 681–684.
- Torquato, S., 2002. *Random Heterogeneous Materials*. Springer, New York.
- Torquato, S., 2002. Statistical description of microstructure. *Annual Review of Materials Research* 32, 77–111.

- Šejnoha, M., Zeman, J., 2002. Overall viscoelastic response of random fibrous composites with statistically quasi uniform distribution of reinforcements. *Computer Methods in Applied Mechanics and Engineering* 191 (44), 5027–5044.
- Walpole, L.J., 1969. On bounds for the overall elastic moduli of inhomogeneous system I. *Journal of the Mechanics and Physics of Solids* 14, 151–162.
- Willis, J.R., 1977. Bounds and self-consistent estimates for the overall properties of anisotropic composites. *Journal of the Mechanics and Physics of Solids* 25, 185–202.
- Willis, J.R., 1986. Variational estimates for the overall response of an inhomogeneous nonlinear dielectric. In: Kohn, R.V., Ericksen, J.L., Kinderlehrer, D., Lions, J.-L. (Eds.), *Homogenization and Effective Properties of Materials and Media*. Springer-Verlag, New York, pp. 245–263.